

# Dynamic Phase Calibration Method for CSI-based Indoor Positioning

Guangxin Wang  
Department of EECS  
Oregon State University  
Corvallis, OR, USA  
wangg@oregonstate.edu

Arash Abbasi  
College of Computer and Cyber Sciences  
Dakota State University  
Madison, SD, USA  
arash.abbasi@dsu.edu

Huaping Liu  
Department of EECS  
Oregon State University  
Corvallis, OR, USA  
huaping.liu@oregonstate.edu

**Abstract**—The demand for location-based services (LBS) increases significantly with the development of smart devices. Their built-in WiFi capability makes WiFi-based approaches essential for a range of indoor positioning applications. In such LBS systems, accessing received signal strength indicator (RSSI) and finer-grained channel state information (CSI) is enabled by modifying commodity WiFi devices. Additionally, multiple-input and multiple-output (MIMO) and orthogonal frequency-division multiplexing (OFDM) provide the spatial and frequency diversity to build the fingerprint database with CSI. However, due to hardware and environmental impacts, such systems suffer from phase errors and fingerprint noise. In this paper, a novel phase calibration method is proposed to reduce the fingerprint noise and improve the accuracy of CSI-based indoor positioning systems. The CSI phase of each subcarrier is extracted from the WiFi access points in a multi-antenna wireless network. First, the phase offset is calculated through the conventional method that uses a linear transformation to remove phase errors. Then, a dynamic phase calibration method is introduced to compensate for the phase offset by tracking the anomalous phase difference between each CSI sample and neighboring subcarrier. Finally, a machine learning algorithm is trained to estimate the target position. The performance of the proposed algorithm is investigated by evaluating the prediction rate from a margin of error (MoE) model and calculating the average distance error between the predicted grid and ground truth. Experimental results show the dynamic phase calibration method outperforms the conventional linear transformation calibration method by a higher prediction rate and improves the average position accuracy.

**Index Terms**—Channel state information, device-free, fingerprinting, indoor positioning, phase calibration

## I. INTRODUCTION

Wireless positioning systems play a significant role in various location-based services (LBS) such as location awareness, navigation, and object tracking. The demand for such services is envisioned to increase drastically as smart applications developing. For outdoor positioning services, global navigation satellite systems (GNSS) like GPS, GLONASS, Galileo, and Beidou provide a reliable solution. The aforementioned GNSS systems are incapable of providing accurate positioning services for most indoor scenarios. However, most human activities occur in indoor environments [1]. For indoor positioning,

various techniques such as ultra-wide band (UWB) [2], [3], Bluetooth [4], radio-frequency identification (RFID) [5], and WiFi [6] have been proposed in the past two decades. Among them, WiFi-based approaches have attracted widespread interest as ubiquitous, low-cost solutions for indoor applications. WiFi-based indoor positioning systems can be categorized into two types: 1) signal propagation approaches, in which propagation parameters such as time of arrival (ToA) [7], [8], time difference of arrival (TDoA) [9]–[12], and angle of arrival (AoA) are measured to estimate the target location; and 2) fingerprinting-based approaches, in which a database is maintained with certain fingerprint features, including received signal strength indicator (RSSI) and channel state information (CSI) to match the target's position. One advantage of fingerprint-based systems is that they are device-free, meaning they can detect an object's position without requiring the object to carry additional hardware.

In the WiFi 802.11 protocol, multiple-input and multiple-output (MIMO) and orthogonal frequency-division multiplexing (OFDM) provide the spatial and frequency diversity, enabling the receiver to access channel information. RSSI is widely used in fingerprint-based schemes because of the simplicity and accessibility to extract the signal strength information. RSSI-based fingerprint method for indoor positioning is introduced in [13] and [14], where the target's position is investigated using a probability model from the RSSI measurements. However, RSSI only provides coarse-grained channel information from the medium access control (MAC) layer. Because RSSI measures the average value of the received data packet, it is sensitive to environmental variations. Study shows that RSSI-based systems achieve an average accuracy of 2 to 4 meters [15]. In contrast, CSI captures fine-grained channel information measured by OFDM subcarriers from the physical (PHY) layer that contains the frequency diversity of the channels. Therefore, the CSI-based method outperforms the RSSI-based approach in positioning accuracy, and system stability [6] [16]. Moreover, CSI approaches are capable of detecting channel fading caused by environmental changes and multipath reflections [17]. In general, comparing to the RSSI-based approach, the finer granularity and low susceptibility to environmental factors make the CSI-based approach a better candidate in fingerprinting systems.

Different features such as phase, amplitude, and the hybrid of both have been investigated in CSI-based fingerprint systems. In [18] and [19], the frequency diversity of OFDM subcarriers is explored, and the sum of CSI amplitudes is used to create the fingerprint database. However, multipath fading limits the accuracy and robustness of this CSI amplitudes approach. The CSI phase is combined with its amplitude to improve performance. FIFS [20] and CSI-MIMO [21] utilize both the CSI amplitude and phase as fingerprints and adopt a probabilistic model to determine the target location without proper phase calibration. To compensate for the phase offset caused by the lack of synchronization between the transmitter and receiver, PinLoc [22], and DeepFi [23] use linear transformation to calibrate the CSI phase. A phase sanitization method is also proposed in PhaseFi [24] to reduce the randomness of the CSI phase. However, the phase offset keeps shifting due to dynamic environmental changes, such as temperature fluctuation and the presence of obstacles.

In this paper, a novel dynamic phase calibration method is proposed to reduce the fingerprint noise and improve the accuracy of CSI fingerprint-based indoor positioning systems. A machine learning algorithm is employed to estimate the target's position. For both the offline and the online stage, the raw CSI phase of each OFDM subcarrier is extracted from a multiple-antenna wireless network using modified firmware on two access points. Then, the extracted phase information is processed with the conventional phase calibration method explained in [24]. This linear transformation method eliminates the phase errors produced on the transmitter and the receiver. To reduce phase errors from environmental changes and object movements, a dynamic phase calibration is introduced to adaptively compensate the offset by tracking the anomalous phase difference between both the CSI sample and the neighboring OFDM subcarrier. For the offline stage, the processed phase information is used to train a 1D convolutional neural network (CNN) with long short-term memory (LSTM) to establish the mapping between the fingerprint database and the corresponding position in the test site. During the online stage, the calibrated CSI phase information is processed through continuous signal measurement. The neural network estimates from the calibrated CSI phase information and provides a prediction of the target's position.

## II. PRELIMINARY

OFDM is commonly used in a variety of communication protocols, including the WiFi standards. In OFDM schemes, data is transmitted and received over multiple orthogonal subcarriers with different frequency spacing. A block diagram of an OFDM system consisting of a transmitter and a receiver is shown in Fig. 1. At the transmitter, input data is modulated and mapped to multiple subcarriers. The inverse fast Fourier transform (IFFT) is performed on each subcarrier, and a cyclic prefix is added to the digital data. Data is then converted by a digital-to-analog converter (DAC) and up-converted to the carrier frequency. At the receiver, the inverse process is performed to recover the data. Before the signal demodula-

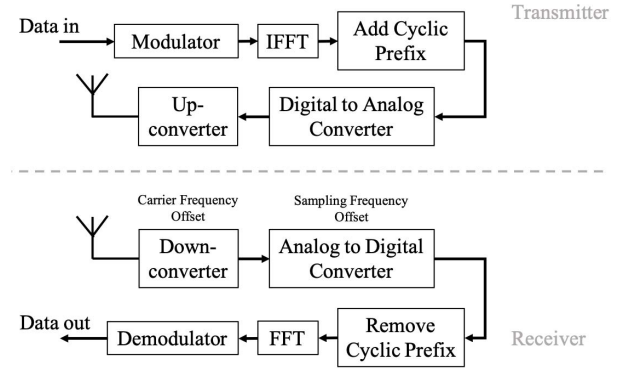


Fig. 1. Block diagram of an OFDM transmitter and receiver.

tion, the equalization process is conducted to compensate for amplitude attenuation and phase error. During this process, the instantaneous CSI is measured by the receiver. Therefore, CSI measurements are available for extraction without any computational overhead. At the subcarrier level, the CSI provides fine-grained information about channel conditions such as scattering, fading, and delay parameters.

A WiFi channel can be described in a flat fading model, which is

$$\mathbf{y} = H\mathbf{x} + \mathbf{n}, \quad (1)$$

where  $\mathbf{y}$ ,  $\mathbf{x}$  and  $\mathbf{n}$  represent the received signal vector, the transmitted signal vector, and the additive white Gaussian noise (AWGN) vector, respectively. In a MIMO-OFDM system,  $H \in \mathbb{C}^{M \times N \times K}$  denotes the channel matrix, where  $M$  and  $N$  are the numbers of transmitter and receiver antennas, and  $K$  is the total number of subcarriers.  $H$  represents the CSI over  $K$  subcarriers that is given as

$$H = [H_1, H_2, \dots, H_K]^T. \quad (2)$$

For  $M \times N$  MIMO antenna streams, let  $\mathbf{H}_k$  defines the CSI matrix of the  $k$ -th subcarrier. It can be written as

$$H_k = \begin{bmatrix} h_{11} & h_{12} & \cdots & h_{1n} \\ h_{21} & h_{22} & \cdots & h_{2n} \\ \cdots & \cdots & \cdots & \cdots \\ h_{m1} & h_{m2} & \cdots & h_{MN} \end{bmatrix}, \quad (3)$$

where  $h_{mn}$  is a complex number representing the CSI of the  $m$ -th transmitter and the  $n$ -th receiver antenna stream.  $h_{mn}$  is defined as  $h_{mn} = |h_{mn}| \exp(j\angle h_{mn})$ , where  $|h_{mn}|$  and  $\angle h_{mn}$  are the amplitude and phase.

## III. SYSTEM CONFIGURATION

In this section, we describe the architecture and the phase calibration process of the proposed system.

### A. System Architecture

The architecture of the proposed system is depicted in Fig. 2. As seen, the CSI is extracted with the commodity WiFi devices. Two TL-WR2543 access points manufactured by TP-Link are used as the transmitter and the receiver.

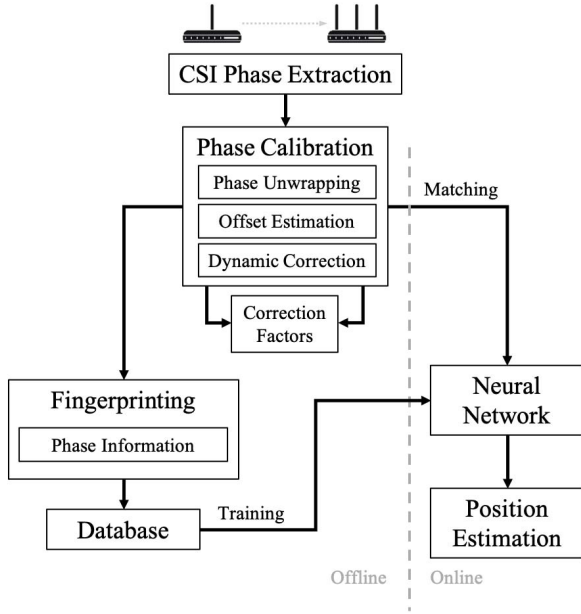


Fig. 2. Architecture of the proposed system.

Each access point has a built-in Atheros network interface card (NIC). The access point can obtain the CSI with modified OpenWrt firmware released by the Atheros CSI Tool [25]. Both access points are remotely controlled to process the data. The system is configured as a  $1 \times 3$  MIMO, with one transmitter and three receiver antennas.

In IEEE 802.11 WiFi protocol, there are 56 subcarriers for the 20 MHz bandwidth and 114 subcarriers for the 40 MHz bandwidth channel, respectively. With the help of the CSI toolkit, the Atheros NIC reports CSI from 56 available subcarriers in a 20 MHz channel [25]. The obtained CSI is represented as  $H \in \mathbb{C}^{1 \times 3 \times 56}$ . In total, 168 CSI data points are collected from one received packet. Unlike RSSI, which only reports one averaged value of each packet, CSI represents the channel response of each subcarrier, which significantly improves the fine granularity of the data samples.

To use the phase information as the fingerprint, the phase pre-processing is conducted on both offline and online stages for the deep learning process. Phase pre-processing includes phase extraction and calibration. The steps of phase calibration comprise phase unwrapping, phase offset estimation, and phase dynamic correction, which are explained in the next section. The fingerprint features are obtained from the processed CSI phase information and stored to train the neural network. In the neural network, the mapping is established between the fingerprint database and the target location. During the online stage, the real-time measurement of the CSI phase is calibrated and used as the input to estimate the target's position from the neural network.

### B. CSI Phase Calibration and Feature Extraction

The purpose of the phase calibration procedure is to obtain a more reliable CSI phase and reduce the fingerprint noise caused by the hardware and environmental fluctuation.

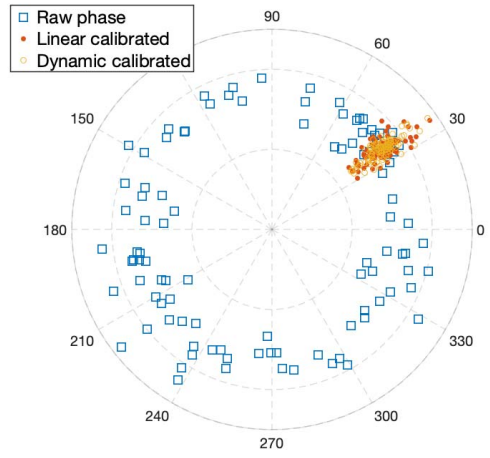


Fig. 3. Raw phase (blue) of 100 CSI measurements, same data after linear calibration (red), and after dynamic calibration (yellow).

The CSI phase measured by the NIC is wrapped, within the range of  $[-\pi, \pi]$ , which differs from the true phase by an integral multiple of  $2\pi$ . The first step of phase calibration is to unwrap the measured phase to restore the appropriate multiples of  $2\pi$ . At the moment of  $\varepsilon$ , for the  $k$ -th subcarrier, let  $\Delta\varphi_{\varepsilon,k} = \varphi_{\varepsilon,k+1} - \varphi_{\varepsilon,k}$  represents the difference between each of two neighboring subcarriers. The unwrapped phase  $\theta_{\varepsilon,k+1}$  is calculated through the following process:

$$\theta_{\varepsilon,k+1} = \begin{cases} \varphi_{\varepsilon,k+1} - 2\pi, & \Delta\varphi_{\varepsilon,k} > \pi \\ \varphi_{\varepsilon,k+1} + 2\pi, & \Delta\varphi_{\varepsilon,k} < -\pi \\ \varphi_{\varepsilon,k+1}, & -\pi < \Delta\varphi_{\varepsilon,k} < \pi \end{cases} \quad (4)$$

There are two primary sources of the phase errors from the hardware of a typical OFDM system (Fig. 1). One is the carrier frequency offset (CFO) generated during the down-conversion at the receiver. Errors can arise during this process when the central frequencies between the transmitter and the receiver are not matched accurately due to non-synchronized local oscillations. The CFO introduces phase errors for all measured subcarriers, regardless of their subcarrier index. Another source of phase error is the sampling frequency offset (SFO) generated by the analog-to-digital converter (ADC). The SFO introduces a time delay, causing the CSI phase errors, which are proportional to the subcarrier index. Thus, the raw CSI phase information has limited usefulness as the fingerprint. The raw CSI must be calibrated before fingerprint information can be extracted.

The measured CSI phase  $\theta_{\varepsilon,k}$  of the  $k$ -th subcarrier at  $\varepsilon$  moment can be expressed as

$$\theta_{\varepsilon,k} = \phi_{\varepsilon,k} + 2\pi \frac{I_k}{N} \tau_{\varepsilon} + \beta_{\varepsilon}, \quad (5)$$

where  $\phi_{\varepsilon,k}$  represents the estimated CSI phase of  $k$ -th subcarrier at  $\varepsilon$  moment,  $I_k$  is the subcarrier index,  $N$  is the fast Fourier transform (FFT) size,  $\tau_{\varepsilon}$  denotes a time delay caused by SFO, and  $\beta_{\varepsilon}$  is an unknown phase offset from CFO.

The total number of OFDM subcarriers for the 20 MHz WiFi channel is  $K = 56$ . To find  $\phi_{\varepsilon,k}$  via conventional phase

calibration, let  $a$  and  $b$  be the linear transformation coefficients that satisfy the following condition.

$$\arg \min_{a,b} \sum_{k=1}^K (\theta_{\varepsilon,k} - aI_k - b)^2. \quad (6)$$

Because the OFDM subcarrier is symmetric, in a simplified derivation [24], those coefficients can be defined as

$$\begin{aligned} a &= \frac{\theta_{\varepsilon,K} - \theta_{\varepsilon,1}}{I_K - I_1}, \\ b &= \frac{1}{K} \sum_{k=1}^K \theta_{\varepsilon,k}. \end{aligned} \quad (7)$$

Fig. 3 shows a set of raw phases from 100 CSI measurements in blue squares and the calibrated phase using the conventional linear transformation method in red dots. This phase calibrated method is stable in a static environment. However, the phase changes drastically in a dynamic environment with object movements. For example, in a 2.4 GHz WiFi band, the phase cycles through a distance of its wavelength of 0.125 m. The phase rotates when the object moves farther than the wavelength distance within a short period. According to (4), during the phase unwrapping process, if the criteria  $|\Delta\varphi_{\varepsilon,k}| > \pi$  or  $|\Delta\varphi_{\varepsilon,k}| < -\pi$  is altered by the phase rotation, an error of  $|\Delta\varphi_{\varepsilon,k}|$  will be introduced. The phase difference can be used to overcome this problem. In the OFDM scheme, the frequency spacing of other subcarriers is evenly distributed. With respect to the first subcarrier, the equivalent wavelength among those subcarriers becomes much longer, which reduces the sensitivity to the object movement in a static environment.

Two metrics are defined: for the  $k$ -th subcarrier, 1) the phase difference between neighboring subcarriers  $\Delta\xi_k$ , and 2) the phase difference between adjacent CSI samples  $\Delta\psi_k$ ,

$$\begin{aligned} \Delta\xi_k &= \phi_{\varepsilon,k+1} - \phi_{\varepsilon,k}, \\ \Delta\psi_k &= \phi_{\varepsilon+\Delta t,k} - \phi_{\varepsilon,k}, \end{aligned} \quad (8)$$

where  $\varepsilon$  is the sampling time, and  $\Delta t$  is the sampling interval. In our configuration, the total number of subcarriers is  $K = 56$ . so the sets of those phase differences are  $\Xi_\varepsilon = \{\Delta\xi_1, \Delta\xi_2, \dots, \Delta\xi_{K-1}\}$  and  $\Psi_\varepsilon = \{\Delta\psi_1, \Delta\psi_2, \dots, \Delta\psi_K\}$ .

To identity any error of  $|\Delta\varphi_{\varepsilon,k}|$  occurred during phase unwrapping,  $\Delta\xi_k$  is smoothed by the following condition:

$$\Delta\xi_k = \begin{cases} \Delta\xi_k, & |\Delta\xi_k| < \sigma |\max(\Xi)| \\ \Delta\xi'_k, & \text{otherwise} \end{cases}, \quad (9)$$

where  $\Delta\xi'_k = \text{avg}(\Xi) + (1 - \delta)\Delta\xi_k$ ,  $\delta$  is the correction factor, and  $\sigma$  defines a threshold of the maximum value. Then, the smoothed  $\Delta\xi_k$  is then added back to restore the calibrated phase  $\phi_{\varepsilon,k+1}$ .

The received data samples are in a sequence of transmitted packets. In consonance with (5) and (8), the phase difference between measured CSI samples is described as

$$\begin{aligned} \Delta\theta_k &= \theta_{\varepsilon+\Delta t,k} - \theta_{\varepsilon,k} \\ &= (\phi_{\varepsilon+\Delta t,k} - \phi_{\varepsilon,k}) + 2\pi \frac{I_k}{N} (\tau_{\varepsilon+\Delta t} - \tau_\varepsilon) \\ &\quad + (\beta_{\varepsilon+\Delta t} - \beta_\varepsilon) \\ &= \Delta\psi_k + 2\pi \frac{I_k}{N} \Delta\tau_k + \Delta\beta_k, \end{aligned} \quad (10)$$

which holds the corresponding phase difference of all the subcarriers between the previous and current packets with  $\Delta t$  interval. In the ideal case, at the packet transmitting interval of a few hundredths of a second, the variation of  $\Delta\tau_j$  and  $\Delta\beta_j$  are minimal, while the phase from the adjacent CSI sample follows a relatively similar trend. Thus,  $\Delta\psi_k$  fits within a small number of phase differences. However, the environment can have a severe impact from one moment to another, which causes phase errors during unwrapping. To mitigate the impact of uncertain phase rotation in equation (10), the slope and intercept point  $(a', b')$  can be solved by satisfying this condition:

$$\arg \min_{a',b'} \sum_{k=1}^K (\Delta\theta_k - a'I_k - b')^2. \quad (11)$$

After linear transformation, the slope  $a'$  indicates the variation of  $\Delta\psi_k$ . Define a confident interval  $\eta$  for slope  $a'$ , when  $a'$  out of the range of  $\eta$ , the measured phase  $\theta_{\varepsilon+1,k}$  that contains the corresponding  $\Delta\psi_k$  is discarded.

Once each measured CSI phase has been updated by the aforementioned phase correction process,  $a$  and  $b$  can be derived from (6). An example of dynamic phase calibration results is shown in Fig. 3 as the yellow circles. Depends on the testing environment, the value of  $\delta$  and  $\eta$  are optimized and maintained in a database as part of the fingerprint. The adaptively calibrated phase information is stored in the database for neural network training.

### C. Neural Network Model

The neural network includes the input layer, the 1-D convolutional neural network (CNN) layers, the long short-term memory (LSTM) layers, the fully connected linear layer, and the output layer. They are  $X \times Y$  positions corresponding to the location grid on the floor, where  $X$  and  $Y$  are the numbers of grids on the horizontal and vertical axis. The input is a matrix  $\phi_\varepsilon \in \mathbb{C}^{M \times N \times K}$  that consist of the CSI phase information, where  $M$  and  $N$  are the numbers of transmitter and receiver antennas, and  $K$  is the number of subcarriers. The convolutional layer acts as a low-level feature extractor, which is applied to reduce the data size and computational complexity. After the convolutional layer, the LSTM and linear layers are used for better network expressiveness of the sequential data.

The neural network is trained by phase information that is labeled with grid index, and using stochastic gradient descent

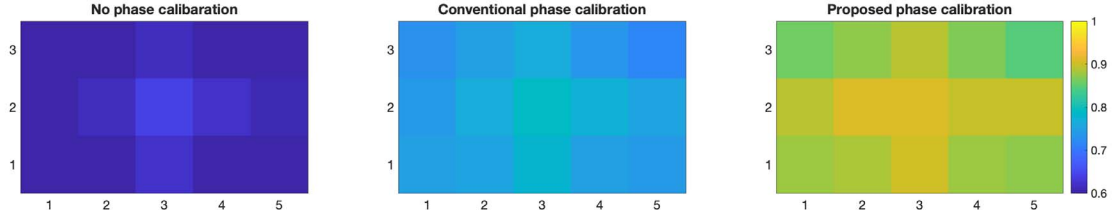


Fig. 5. MoE prediction rate per grid by different phase dataset: (a) dataset #1: Unwrapped raw phase. (b) dataset #2: Conventionally calibrated phase (c) dataset #3: Dynamically calibrated phase.

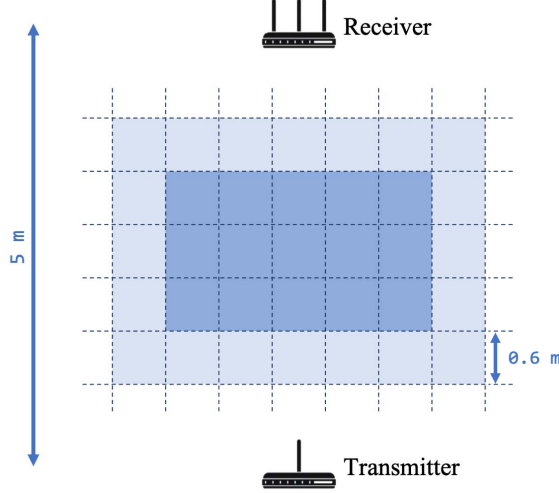


Fig. 4. Testsite topology: transmitter, receiver, and floor grid placement.

with the negative log likelihood (NLL) loss function shown in (12).

$$\text{Loss} = - \sum_{i=0}^P \sum_{j=0}^Q t_{i,j} \ln(T_{i,j}), \quad (12)$$

where  $P$  is the batch size of the stochastic gradient descent and  $Q$  is the number of classifiers.  $t_{i,j}$  and  $T_{i,j}$  are the ground truth vector and predicted vector of the probability distribution. The number of epochs impacts the performance of the network model, respectively. An epoch is selected from the best validation results before overfitting occurs. The system predicts the result by finding the class with the greatest softmax output.

#### IV. EXPERIMENTS

Fig. 4 shows the setup of the experiment system. The testing field is a 7 m × 6 m area with the grids marked on the floor. Each grid is approximately 0.6 m × 0.6 m. A total of 15 grids (rendered as a darker blue area in Fig. 4) in the central area comprise the core testing site to evaluate the system performance. The light blue areas are secondary areas for analyzing positioning errors.

The transmitter and receiver are placed on the short sides of the testing field. They are set 5 m apart and directly facing each other. The transmitter and receiver are mounted on a platform that is 1.2 m above the floor. A person moves among the center of each grid to gather the data at each location.

TABLE I  
PREDICTION RATE AND POSITION ERROR ACROSS DATASETS.

	Data #1	Data #2	Data #3
Predicted rate (%)	60.1	75.2	88.4
Averaged error (m)	2.35	1.69	1.33

Position performance is analyzed by the successful prediction rates and failure prediction rates with a margin of error (MoE) model. The MoE model considers any predicted grid that lands on a surrounding grid as a successful prediction. Grids that are close to the ground truth are more likely to be predicted as being occupied. Even without a defined explicit distance metric in the loss function, the network model learns features relevant to the regions of interest. The results include both successful prediction and failure prediction are adopted to evaluate positioning accuracy. The position error is calculated by averaging the distance between the predicted grid and the actual grid, regardless of the MoE model.

The system is evaluated from three different sets of fingerprints: the unwrapped raw phase, the conventional linear fitted phase, and the dynamically calibrated phase. The heat map shown in Fig. 5 suggests that the proposed phase calibration method has a higher overall success rate than the conventional linear calibration and non-calibration methods. Within the test site, the successful prediction rate is highest in the central area and gradually degrades to the corners. Table I compares the overall prediction rates and average position errors across three datasets. The dynamic calibrated CSI phase reaches an 88.4% successful rate, while the prediction rates of the unwrapped raw CSI phase and the linear calibrated phase are 60.1% and 75.2%, respectively. The average position errors of those three datasets are 2.35 m, 1.69 m, and 1.33 m. Comparing to the conventional linear transformation method, the proposed phase calibration method improves the prediction rate by 13.2% and reduces the average position error from 1.69 m to 1.33 m by 21.3%.

#### V. CONCLUSIONS

In this paper, two commodity wireless access points with built-in Atheros NIC were utilized for CSI phase extraction. A novel phase calibration method was proposed, which introduced two phase correction factors to improve the phase calibration process dynamically. A multi-layer neural network was trained to estimate the target's position. The results where evaluate both the prediction rate in an MoE model and the average position error illustrated that the use of

the conventional linear transformation calibration method was suffered from a drop in prediction rate and, therefore, a lower position accuracy. For the CSI-based positioning system, the proposed method outperformed the conventional linear transformation calibration method by 13.2% higher prediction rate and reduces the average position error 21.3%.

## REFERENCES

- [1] A. Makki, A. Siddig, M. Saad, and C. Bleakley, "Survey of WiFi positioning using time-based techniques," *Computer Networks*, vol. 88, pp. 218–233, 2015.
- [2] A. Alarifi, A. Al-Salman, M. Alsaleh, A. Alnafessah, S. Al-Hadhrani, M. A. Al-Ammar, and H. S. Al-Khalifa, "Ultra wideband indoor positioning technologies: analysis and recent advances," *Sensors*, vol. 16, no. 5, May 2016.
- [3] R. Ye, S. Redfield, and H. Liu, "High-precision indoor UWB localization: Technical challenges and method", in *Proc. IEEE ICUBW'10*, Nanjing, China, Sep. 2010.
- [4] S. Feldmann, K. Kyamakyia, A. Zapater, and Z. Lue, "An indoor Bluetooth-based positioning system: Concept, implementation and experimental evaluation," 01 2003, pp. 109–113.
- [5] A. Lim and K. Zhang, "A robust RFID-based method for precise indoor positioning," in *Proc. Int Conf. Industrial, Engineering and Other Applications of Applied Intelligent Systems*, 2006, pp. 1189–1199.
- [6] Z. Yang, Z. Zhou, and Y. Liu, "From RSSI to CSI: Indoor localization via channel response," *ACM Comput. Surv.*, vol. 46, no. 2, Dec. 2013.
- [7] T. Qiao and H. Liu, "An improved method of moments estimator for TOA based localization," *IEEE Communications Letters*, vol. 17, no. 7, pp. 1321–1324, Jul. 2013.
- [8] T. Qiao and H. Liu, "Improved least median of squares localization for non-line-of-sight mitigation," *IEEE Communications Letters*, vol. 18, no. 8, pp. 141–144, Aug. 2014.
- [9] T. Qiao, S. Redfield, A. Abbasi, Z. Su, and H. Liu, "Robust coarse position estimation for TDOA localization," *IEEE Wireless Communications Letters*, vol. 2, no. 6, pp. 623–626, Dec. 2013.
- [10] Y. Zou, H. Liu, and Q. Wan, "An iterative method for moving target localization using TDOA and FDOA measurements," *IEEE Access*, vol. 6, pp. 2746–2754, Feb. 2017.
- [11] Z. Su, G. Shao, and H. Liu, "Semidefinite programming for NLOS error mitigation in TDOA localization," *IEEE Communications Letters*, vol. 22, no. 7, pp. 1430–1433, July 2018.
- [12] Y. Zou, H. Liu, W. Xie, and Q. Wan, "Semidefinite programming methods for alleviating sensor position error in TDOA localization," *IEEE Access*, vol. 5, pp. 23111–23120, Sep. 2017.
- [13] P. Bahl and V. N. Padmanabhan, "Radar: an in-building RF-based user location and tracking system," in *Proc. IEEE INFOCOM 2000*, vol. 2, 2000, pp. 775–784.
- [14] M. Youssef and A. Agrawala, "The Horus WLAN location determination system," in *Proc. 3rd Int. Conf. Mobile Systems, Applications, and Services*, 2005, New York, NY, pp. 205–218.
- [15] P. Kumar, L. Reddy, and S. Varma, "Distance measurement and error estimation scheme for RSSI based localization in wireless sensor networks," in *Proc. 2009 Int. Conf. Wireless Communication and Sensor Networks (WCSN)*, 2009, pp. 1–4.
- [16] Y. Zhuo, H. Zhu, H. Xue, and S. Chang, "Perceiving accurate CSI phases with commodity WiFi devices," in *Proc. IEEE INFOCOM*, 2017, pp. 1–9.
- [17] A. Bhartiya, Y.-C. Chen, S. Rallapalli, and L. Qiu, "Harnessing frequency diversity in WiFi networks," in *Proc. 17th Annual Int. Conf. Mobile Computing and Networking (MobiCom)*, New York, NY, 2011, pp. 253–264.
- [18] K. Wu, J. Xiao, Y. Yi, D. Chen, X. Luo, and L. M. Ni, "Csi-based indoor localization," *IEEE Trans. Parallel and Distributed Systems*, vol. 24, no. 7, pp. 1300–1309, 2013.
- [19] Q. Song, S. Guo, X. Liu, and Y. Yang, "CSI amplitude fingerprinting-based NB-IoT indoor localization," *IEEE Internet of Things Journal*, vol. 5, no. 3, pp. 1494–1504, 2018.
- [20] J. Xiao, K. Wu, Y. Yi, and L. M. Ni, "FIFS: Fine-grained indoor fingerprinting system," in *Proc. 2012 Int. Conf. Computer Commun. and Networks (ICCCN)*, 2012, pp. 1–7.
- [21] Y. Chapre, A. Ignjatovic, A. Seneviratne, and S. Jha, "CSI-MIMO: Indoor WiFi fingerprinting system," in *Proc. 39th Annual IEEE Conf. Local Computer Networks*, 2014, pp. 202–209.
- [22] S. Sen, B. Radunovic, R. R. Choudhury, and T. Minka, "You are facing the Mona Lisa: Spot localization using PHY layer information," in *Proc. 10th Int. Conf. Mobile Systems, Applications, and Services (MobiSys'12)*, New York, NY, 2012, pp. 183–196.
- [23] X. Wang, L. Gao, S. Mao, and S. Pandey, "Deepfi: Deep learning for indoor fingerprinting using channel state information," in *Proc. IEEE WCNC*, 2015, pp. 1666–1671.
- [24] X. Wang, L. Gao, and S. Mao, "Phasefi: Phase fingerprinting for indoor localization with a deep learning approach," in *Proc. IEEE GLOBECOM*, 2015, pp. 1–6.
- [25] Y. Xie, Z. Li, and M. Li, "Precise power delay profiling with commodity WiFi," in *Proc. 21st Annual Int. Conf. Mobile Computing and Networking*, New York, NY 2015, p. 53–64.